PHYSICAL REVIEW E VOLUME 52, NUMBER 6 DECEMBER 1995

Quantum molecular dynamics simulations of hot, dense hydrogen

L. Collins, I. Kwon, and J. Kress
Theoretical Division, Los Alamos National Laboratory, Los Alamos, New Mexico 87545

N. Troullier
Minnesota Supercomputer Institute, University of Minnesota, Minneapolis, Minnesota 55455

D. Lynch
Thinking Machines Corporation, Cambridge, Massachusetts 02142

(Received 7 November 1994; revised manuscript received 31 July 1995)

Quantum molecular dynamics simulations of pure samples and of mixtures of isotopic hydrogenic species (H, D, T) yield important structural, dynamical, and electronic properties that characterize matter at high compressions ($\rho \geq 0.25$ g/cm^3) and moderate temperatures (3000–60 000 K). Quantum mechanical treatments of the electrons, contained in periodically replicated reference cells of N_a atoms, by density functional and tight-binding methods determine the force on the nuclei and the electronic structure of the medium. The nuclei move according to the classical equations of motion in response to this quantal force. In addition, pair potentials based on Thomas-Fermi models (Moliere) extend both the temperature and density range of the more sophisticated models. Comparisons of the models are presented together with a comprehensive description of the techniques. Examples over a broad temperature and density range illustrate the basic physics for a hot, dense hydrogen medium.

PACS number(s): 61.20.Ja, 36.40.−c, 82.20.Wt

I. INTRODUCTION

Dense hydrogen (H) exists in highly diverse and rather exotic environments [1–6]. For example, the interiors of brown dwarf stars [5,6] and of gas-giant planets [6,7] such as Jupiter and Saturn consist primarily of hydrogen at high compressions ($\rho \leq 5$ g/cm^3) for moderate temperatures (10^4 K) and exist just below the threshold of sustained thermonuclear fusion. Models of such objects rely heavily on the equation of state of hydrogen in these extreme domains. In the same astrophysical vein, understanding of the evolution and crystallization of white dwarfs hinges on quantum mechanical modifications to the usual classical one-component plasma theory for such dense stars [8]. For more terrestrial applications, capsules for inertial confinement fusion (ICF), which contain mixtures of hydrogenic isotopes, experience implosions to many times solid density ($\rho \gg 1$ g/cm^3) at temperatures on the order of millions of degrees (~ 1 keV). Experiments [9] to date have reached densities of a few g/cm^3; however, ignition requires compressions of hundreds of times larger. In addition, impurities of such species as chlorine provide diagnostics of the physical conditions within the capsule through spectroscopic observations. At high densities, the surrounding H atoms greatly distort the basic atomic character of the impurity, having profound consequences on such measured properties as line broadening. Other devices such as pulsed-power and explosive generators [10,11] also produce materials at very high densities. The latter device has compressed hydrogen almost adiabatically to several g/cm^3 at very low temperatures. The experiment also measured the onset of electrical conductivity, possibly indicating the attainment of an atomic metal phase. Finally, sonoluminous cavities [12], spherically compressed by acoustical waves in liquids, yield very high densities and temperatures and may provide an interesting environment for examining dense plasmas. Therefore, a detailed understanding of the properties and dynamics of dense hydrogen becomes critical to modeling an extensive array of objects and devices.

Since we have presented a detailed historical development in an earlier paper [13], we concentrate on brief descriptions of some of the important models for treating hot, dense hydrogen. The earliest simulations centered on the one-component plasma (OCP). This purely classical model [14,15] consists of point ions of charge $Z_i e$ moving in a uniform background of negative charge so that the total system exhibits electrical neutrality. A coupling constant Γ [$= Z_i e^2/(r_s k_B T_i)$] characterizes many of the properties of the system by a simple ratio of the thermal energy of the ions ($k_B T_i$) at an average ionic temperature T_i to the average Coulombic repulsion between ions ($Z_i e^2/r_s$) at a representative separation given by the ion sphere radius r_s [$=3/(4\pi\rho_i)$] for a given ionic number density ρ_i with k_B, the Boltzmann constant. Despite the wide applicability of the OCP, certain regimes present problems, especially at high densities in which the atomic charge clouds overlap and at moderate temperatures with only partial ionization. Extensions based on two-component models and screening [4] extend somewhat the range of validity; however, in these regimes, the electrons display distinctly quantum mechanical behavior. These effects are best introduced by a direct solution to the Schrödinger equation.

1063-651X/95/52(6)/6202(18)/$06.00

Several quantum mechanical approaches have evolved over the past ten years, basically dividing into two groups. The first treats a single atom but perturbs the atomic potential by effects of the surrounding medium. The description of the medium ranges in complexity from simple potentials [16] to elaborate interactions [17] based, for example, on a hypernetted chain. In turn, molecular dynamics (MD) calculations, incorporating an effective ion two-body potential derived from this "dressed" atom picture, determine properties such as diffusion and viscosity. The other approach represents all the interactions within a sample of N_α atoms on an equal footing. Early calculations [18,19] dealt with static ensembles to determine basic electronic and radiative properties. The next step involved an integrated scheme for treating the electronic and nuclear motion. Both quantum Monte Carlo [20] and molecular dynamics [21–26] simulations incorporate the two types of motion. In the MD procedure, a quantum mechanical (QM) treatment of the electrons yields a force on the ions, which then move according to the classical equations of motion. The QM approaches cover a wide variety of schemes, including semi-empirical methods such as tight-binding [13,25], Thomas-Fermi [24], Hartree-Fock [21] and density functional [22,23,25]. These treatments have been applied principally at very high [24] or very low temperatures for weakly to highly compressed hydrogen systems. Recently, the quantum molecular dynamics (QMD) methods [22,23,25] have been extended into the intermediate regime in order to test the range of validity of many of the approximate approaches.

In fact, this intermediate regime for hydrogen and its isotopes shall occupy our primary attention. We consider compressions of over a factor of fifty, representing a transition from molecular liquid (ρ=0.0625 g/cm^3) to very dense atomic fluid ($\rho \leq 5$ g/cm^3) and temperatures from near thermal ($T \approx 0.1$ eV) to tens of thousands of degrees ($T_i \leq 10$ eV). The denizens of this regime range from molecules to atoms to positive and negative ions. Due to this diversity, exploration of this realm must take place at the most sophisticated level in which all types of interactions receive equal treatment. The physical situations examined here reside in the great variety of objects and devices mentioned above, making an understanding critical to refinement, improvement, and scaling [27]. To this end, we describe simulations of hydrogen using QMD techniques within a finite-temperature density functional approach. The formalism is discussed in Sec. II, followed by a detailed examination of hydrogen over a range of temperatures and densities in Sec. III. Unless otherwise noted, atomic units (a.u.) apply throughout (1 hartree = 2 Ry).

II. FORMALISM

We consider as a model of a hot, dense medium a collection of N_a nuclei and N electrons in a cubic reference cell of length L. The time-dependent (TD) Schrödinger equation governs the interactions and evolution of such a system. However, to perform such calculations on reasonable size samples would require immense computational resources. Path integral techniques have been applied to equilibrium simulations of protons and electrons [28], and in principle, require less computational investment than the solution of the TD Schrödinger equation. To date, most applications have covered only small systems and classical interaction potentials [29]. To obtain a more tractable problem, we make the Born-Oppenheimer approximation by which the nuclear and electronic motion decouple. We divide the evolution of the system into two stages. For a fixed nuclear configuration, a fully quantum mechanical treatment applies to the electrons. From an elaborate electronic structure calculation, we determine the force of each nuclei. This force in turn is used in the classical equations of motion to advance the nuclei [30]. Repeating this procedure for each time step systematically advances the system. We shall in the following sections describe in detail the basic parts of this quantum molecular dynamics scheme.

A. Molecular dynamics

Once the quantum mechanical forces $\boldsymbol{F}_\alpha$ on each ion are determined, the particles are advanced temporally by solving the classical equations of motion

$$m_\alpha \ddot{\boldsymbol{r}}_\alpha = \boldsymbol{F}_\alpha, \tag{1}$$

where m_α is the mass of the αth nuclei and $\ddot{\boldsymbol{r}}_\alpha$ is its acceleration. We solve these equations by a standard velocity Verlet technique [30], which yields third-order accuracy in the positions and second-order in the velocities. Repeating the two-step process of quantum mechanical evaluation of the forces for a fixed nuclear configuration and of moving the nuclei according to classical MD, we evolve the system in time by determining positions and velocities at each step. The collection of these coordinates and velocities forms a trajectory from which various bulk and thermodynamical properties can be extracted. Most of these properties arise from the association of various autocorrelation functions through Green-Kubo formulation [30–32].

All of our simulations employ constant density and volume. Since we employ a finite sample in a basic reference cell, we also invoke periodic boundary conditions by which a particle exiting the cell through one side is replaced by one entering on the opposite side. This convention preserves constant density within the cell. We do consider both microcanonical and isokinetic ensembles. In the former, the system remains free to adjust to an average equilibrium ionic temperature T_i, and the total energy should be conserved. The degree to which energy conservation obtains provides an excellent diagnostic of the MD parameters, especially the time step. For the isokinetic ensemble, we fix the temperature at a prescribed value T_i. We maintain this balance through a simple velocity scaling procedure [30]. At designated time steps, we scale the calculated velocities as

$$\boldsymbol{v}_{\rm new} = \left[\frac{T_i}{T_K}\right]^{1/2} \boldsymbol{v}_{\rm old}, \tag{2}$$

with the average kinetic temperature T_K given by

$$T_K = \frac{1}{3k_B N_a} \sum_{i=1}^{N_a} m_i v_i^2 \tag{3}$$

and determined from $\mathbf{v}_{\text{old}}$. We primarily focus our attention on a hydrogen medium at a prescribed temperature and density in order to consistently compare various models and regimes. For this case, the isokinetic form provides the most efficient choice while producing reliable properties since a given initial condition requires only a single trajectory run. We start the sample in a high symmetry state such as body-centered cubic (bcc) or face-centered cubic (fcc) and associate with each nucleus a random velocity consistent with a Maxwell-Boltzmann distribution at T_i. Successive application of the Verlet algorithm evolves the system in time. The resulting collection of positions, velocities, and forces of the nuclei at each time step defines a trajectory. In turn, Green-Kubo formulas, based on autocorrelation functions, relate the trajectory information to microscopic properties of the system such as diffusion and viscosity. While autocorrelation functions provide the basis of many such properties, we shall focus on only a few representative quantities with the understanding that the same trajectories can be employed to calculate related properties.

One of the important properties of interest is diffusion. The self-diffusion coefficient D_s for species s can be determined either from the mean-square displacement or velocity autocorrelation function [30] as

$$\begin{aligned} D_s &= \frac{1}{6t}\langle |\boldsymbol{r}_i(t) - \boldsymbol{r}_i(0)|^2 \rangle, \\ D_s &= \frac{1}{3}\int_0^\infty dt \langle \boldsymbol{v}_i(t) \cdot \boldsymbol{v}_i(0) \rangle, \end{aligned} \tag{4}$$

where i designates a particle of the species of type s and the angular brackets denote an average over the particles of species s. For binary mixtures, the mutual diffusion becomes important and has the form [33,34]

$$D_{12} = k_B T \left[\frac{c_1}{m_2} + \frac{c_2}{m_1} \right] \int_0^\infty Z_{12}(t) dt, \tag{5}$$

where

$$Z_{12}(t) = \frac{\langle \boldsymbol{J}(t) \cdot \boldsymbol{J}(0) \rangle}{\langle [\boldsymbol{J}(0)]^2 \rangle}, \tag{6}$$

with the interdiffusion current defined by

$$\boldsymbol{J}(t) = c_2 \sum_i \boldsymbol{v}_{i1}(t) - c_1 \sum_j \boldsymbol{v}_{j2}(t), \tag{7}$$

and m_i and c_i, the mass and molar concentration, respectively of species i.

We can glean insights into the structure of the medium by determining the pair correlation function $g(r)$, which gives the probability of finding a particle at a distance r from a reference particle [30]. Similar pair correlation functions can be constructed for binary mixtures involving the same (g_{11}, g_{22}) or different species g_{12}. This function gives an average description of the relative position of particles in the medium. The basic nature of a medium, whether liquid or solid, arises from consideration of the translational-order parameter $\rho(k,t)$ [30] with k the magnitude of a reciprocal lattice vector for the initial lattice. By monitoring this function over time, we can ascertain the nature of the simulated medium. Related to the pair distribution function by a Fourier transform is the structure factor $S(k)$, which gives the Fourier components of the density fluctuation of the medium.

B. Density functional

Since the general features of our approach are discussed in extensive detail in several comprehensive texts [35] and review articles [36], we shall give only a brief description of the basic formulation and concentrate on the specific details. In order to introduce finite electron temperature ($T_e > 0$) effects into the density functional formulation, we follow the basic derivation of Mermin [37]. The functional becomes

$$\Omega[\psi_i] = E[\psi_i] - T_e S, \tag{8}$$

where S is the entropy and $E[\psi_i]$ is the usual Kohn-Sham functional at $T_e = 0$ adjusted by a density of

$$n(\boldsymbol{r}) = \sum_i f_i |\psi_i(r)|^2 \tag{9}$$

with f_i determined by the Fermi distribution function. For an ideal Fermi gas, the entropy becomes simply

$$S = -k_B \sum_i [f_i \ln f_i + (1 - f_i) \ln(1 - f_i)]. \tag{10}$$

By employing the Mermin free energy Ω as the conservation quantity, instead of the total energy, the forces arise simply from [38]

$$\boldsymbol{F}_\alpha = -\boldsymbol{\nabla}_\alpha \Omega. \tag{11}$$

The standard Kohn-Sham (KS) total energy functional $E[\psi_i]$ in atomic units (a.u.) for a set of doubly occupied orbitals $\{\psi_i\}$ has the form

$$E[\psi_i] = T_S[n] + E_H[n] + E_{\text{ext}}[n] + E_{\text{xc}}[n] + E_{\text{ion}}. \tag{12}$$

The first term represents the kinetic energy functional, the second gives the Hartree functional, which characterizes the Coulombic interaction energy of a classical charge distribution, the third term corresponds to the energy due to the interaction with an external potential, usually the electron-ion interaction, and the fourth term gives the contribution from exchange and correlation effects. We also make the local density approximation (LDA). Finally, the ion-ion term E_{ion} involves a simple Coulombic interaction among the nuclei.

Minimizing the energy functional with respect to variations of the density and subject to the constraint $\int n(\boldsymbol{r}) d\boldsymbol{r} = N$ leads to equations for the orbitals of the Kohn-Sham form

$$\left[-\frac{1}{2}\boldsymbol{\nabla}^2 + V_{\text{ext}}(\boldsymbol{r}) + V_H(\boldsymbol{r}) + V_{\text{xc}}(\boldsymbol{r})\right]\psi_i(\boldsymbol{r}) = \epsilon_i\psi_i(\boldsymbol{r}), \tag{13}$$

where the exchange-correlation potential results from the formal functional derivative of E_{xc} with the density modified by Eq. (9). Since terms in the equations depend on the density and therefore the orbitals, these equations must be solved iteratively. We separate the function ϵ_{xc} into exchange and correlation contributions with the exchange part, based on the free electron gas, taking a form proportional to the cube root of the density. For the correlation term, we employ the Perdew-Zunger parametrization [39] based on the Ceperley-Alder Monte Carlo calculations [40].

The remaining term to specify involves the interaction with an external potential. For an all-electron calculation, this form becomes simple, being the interaction of an electron with the bare nuclei ($\sum_\alpha Z_\alpha|\boldsymbol{r} - \boldsymbol{R}_\alpha|^{-1}$). However, in most practical situations, such all-electron representations become intractable. The strategy employed rests with a treatment of the valence electrons exactly and with a representation of the core electrons by an effective pseudopotential. We have used the Troullier-Martins pseudopotential [41] extended to nonlocal form by the Kleinman-Bylander prescription [42]. We should note that even for hydrogen we have found the pseudopotential form valuable. Using a small cutoff radius affects only slightly the basic properties and effectively removes the cusp condition, significantly reducing the number of plane waves needed for convergence.

We solve the KS equations for a representative supercell of length L of N_a nuclei and N electrons, replicated throughout space to represent the extended medium. Within the reference cell, the atoms may assume any configuration from crystalline to disordered. Invoking Bloch's theorem, the one-electron orbitals become the product of two terms: (1) a simple plane wave that depends on $\mathbf{k}$ and (2) a function that exhibits periodic behavior with respect to the image cells. We expand this cell-periodic function in a plane-wave basis [36] in terms of the reciprocal lattice vector $\mathbf{G}$ and obtain a matrix representation of the KS equations for a given $\boldsymbol{k}$ vector. Since we generally employ spatial cells of extended size, we can accurately perform the matrix-element integrals at a single point, $\boldsymbol{k}$=(0,0,0) or Γ point in k space. Technically, the order of these matrix equations is infinite. In order to place them in a more tractable form, we truncate the plane-wave expansion at a finite cutoff value E_{cut} ($= \frac{1}{2}|\boldsymbol{G}_{\text{cut}}|^2$). We must, of course, successively increase $\boldsymbol{G}_{\text{cut}}$ until convergence in certain properties, for example, the total energy, is attained.

At each step, we solve the KS equations self-consistently, using a quasi-Newton method with Broyden [43] updating of the Jacobian by which only relevant parts are changed and stored. In addition, to ensure that each step provides an improvement, we include backtracking and auto-restarts. For each self-consistency step, we must diagonalize the matrix, using a preconditioned version of the Lanczos method. The technique closely resembles the generalized Davidson approach [44] in which all manipulations of the Hamiltonian matrix remain linear. Finally, for the MD calculations, we need the force experienced by each nuclei. We determine this force by differentiating the total energy expression. For plane waves, the Pulay corrections due to changes in the eigenvectors with position remain zero, a considerable advantage of this basis.

C. Semiempirical potential

While the density functional local density approximation (DF-LDA) method described in the previous section allows a sophisticated treatment of the basic electron and ion interactions, the computational time necessary to evolve long trajectories for large samples of atoms becomes prohibitive. Therefore, to test sample-size effects and the accuracy of thermodynamic and bulk properties, we have developed a semiempirical potential based on a tight-binding (TB) prescription [45,46].

In the tight-binding formulation, the Hamiltonian governing the atomic motions has the general form

$$H = K_i + \sum_n \langle\psi_n|H_{\text{TB}}|\psi_n\rangle + \sum_{i>j}\phi(R_{ij}). \tag{14}$$

The first term represents the kinetic energy of the ions while the second gives the electronic energy calculated from a sum over the occupied eigenenergies of a TB Hamiltonian H_{TB}. The last term, a pairwise potential, provides for the ion-ion repulsion as well as a double-counting correction. In order to produce an effective model of the hydrogenic medium, we must construct a suitable representation of the TB matrix elements. We begin with a two-function basis on each atomic site consisting of $1s$ and $1s'$ orbitals. Fits to diatomic and bulk properties produce the desired functional forms for these matrix elements. The details of the construction and table of parameters for our hydrogenic TBss' potential appear elsewhere [26]. The main reason for exerting all this effort to generate a ss' potential stems from the need to model a dense, broad eigenspectrum that will be populated at high temperatures. Finally, we determine the force acting on a given nucleus by simply taking the negative of the coordinate derivative of the TB potential.

For MD calculations at low temperatures, a simple double population (spin degeneracy) of the lowest-lying energy levels serves to establish the energy and force in the TB approach. However, as the temperature increases, excited and continuum states become populated. In order to include this effect, we employ an approximation based on local thermodynamic equilibrium (LTE). In this case the electron temperature T_e equals the ionic temperature T_i derived directly from the MD ionic kinetic energy ($\frac{1}{2}\sum_\alpha m_\alpha v_\alpha^2$). We then use this temperature in a Fermi-Dirac distribution

$$f(\epsilon_n, T) = \{1 + \exp[-\beta(\epsilon_n - \epsilon_F)]\}^{-1}, \tag{15}$$

where ϵ_n represents an eigenenergy of the TB Hamiltonian and $\beta \equiv k_B T_e$. The Fermi energy ϵ_F must be determined iteratively subject to the constraint that the total number of electrons remains constant:

$$2 \sum_n \int f_n(\epsilon_n, T) d\epsilon = N. \tag{16}$$

Once ϵ_f is determined, the FD distribution fixes the occupation numbers, which are inserted into the form of the TB energy. Since the force depends on this energy, these excited and continuum levels become folded into its calculation.

D. Pair potentials

We also consider modeling the dense media by a simple pair potential. Forms for such potentials abound; however, we select the Moliere expression [47], which falls within a category of models based on the Thomas-Fermi electronic screening function. Since this function poorly represents the actual atomic charge distribution at large distances, a finite truncation is introduced to make the Moliere form more physical. The potential in atomic units is given by

$$\phi(R_{ij}) = \left(\frac{1}{R_{ij}}\right) \sum_{\alpha=1}^{3} E_\alpha(R_{ij}), \tag{17}$$

where

$$E_\alpha(r) = (A_\alpha Z_1 Z_2) \exp\left[-b_\alpha \left(\frac{r}{a_F}\right)\right], \tag{18}$$

with Z_i the nuclear charge on the ith species and $a_F = 0.885[Z_1^{1/2} + Z_2^{1/2}]^{-2/3}$ in bohr. The following numerical coefficients are selected to give the best fit to the Thomas-Fermi (TF) function: A_1=0.35, A_2=0.55, and A_3=0.10; b_1=0.3, b_2=1.2, and b_3=6. For isotopic hydrogenic systems, we take Z_1 and Z_2 to be unity. The potential has several shortcomings: the most notable being its lack of molecular binding, which applies to the standard TF formulation as well. Therefore, its principal applications should pertain to high densities and temperatures.

Having pursued a lengthy sojourn through formalism, we launch into a description of the basic results of these detailed quantum molecular dynamics simulations.

III. RESULTS AND DISCUSSION

A. Tests

We have checked the techniques and programs against a variety of other calculations. Simulations using simple pair potentials validated the classical MD and trajectory analysis programs. For single species, we obtain excellent agreement with the Lennard-Jones (LJ) spline results of Erpenbeck [48] and He-He findings of Younger [21], who employed the analytical expression of Aziz and Slaman [49]. The latter calculations explored the realm of high densities ($\rho \leq 8$ g/cm^3) and temperatures ($T_i \leq 5$ eV). In addition, truncated LJ forms, representing Ar/Kr systems near the triple point, provided excellent benchmarks for mixtures [33,34].

We have tested the LDA programs in a variety of ways. First, we started H_2 at nonequilibrium distances and quenched the system by gradually drawing out energy. We found that the system in the T_i=0 limit attained the proper equilibrium separation of 1.42 bohr. Second, we obtained excellent agreement for pair-correlation functions and diffusion coefficients with other results for the alkali liquid metals, Li and Na, in the regime between melt and boiling [50]. We employed a microcanonical ensemble for the Li simulations and found total-energy conservation to better than 1 part in 10^4 with no perceptible drift. The alkali metals provide an excellent check of the hydrogenic systems since they consist of a single electron outside of a tightly closed shell. Finally, we have compared to other LDA calculations of H, principally at low T_i to excellent effect as discussed in more detail below.

B. General parameters and analysis

Before delving into a detailed description of dense hydrogen, we briefly delineate some basic parameters, common to many of the calculations, and present an example of the trajectory analysis procedure.

1. Potential and forces

For H in the DF-LDA, the pseudopotential has an exact form ($1/r$). However, to converge the total energy for the exact case requires a substantial plane-wave basis with E_{cut} exceeding 100 Ry. Such large bases imply large computational times. The slow convergence in basis arises from the difficulty in representing the cusp condition at the nuclear sites. We circumvent this difficulty by generating a Troullier-Martins pseudopotential for H with a cutoff inside a radius r_c that removes the offending cusp constraint. Fortunately, the properties under investigation remain fairly insensitive to the choice of r_c. We have examined cutoff radii between 0.3 and 1.6 bohr. As long as the pseudopotential truncation remains comparable to the effective interaction range, crudely approximated by twice the ion sphere radius r_s, we observe little difference in the properties compared to the exact $1/r$ form. For example, in the diatomic molecule, the pseudopotential model (r_c=1.4 bohrs) yields a force constant and equilibrium internuclear distance that lie within 4% and 2%, respectively of the all-electron ($1/r$) result for a box of length 12.5 bohrs. Changing E_{cut} from 36 to 64 Ry resulted in a change in the third significant figure for these quantities. We recall that the internuclear separations in the diatomic correspond to nearest-neighbor distances ($\sim 2r_s$) far smaller than those encountered in the bulk simulations in this paper, and therefore, the molecule provides a useful guide for selecting the truncation parameter.

As another test of the LDA programs and pseudopotential representation, we present in Table I the total energy per atom as a function of the ion sphere radius r_s for H in a bcc lattice with a pseudopotential cutoff of 0.3 bohr, a k-space sampling of 145 points, and a plane-wave truncation of 36 Ry. We find less than an 1 mRy difference between 145 and 897 k points in determining the integration within the Brillouin zone and between an r_c of 0.3 bohr and the exact $1/r$ pseudopotential form. Our minimum in the total energy at 1.675 bohrs agrees with Barbee and Cohen [51]. In addition, the values of the total energy per atom in the two approaches differ in the fifth significant figure. For an r_c of 1.4 bohrs at r_s^0 (the ion sphere radius at the energy minimum) we obtain a value of -1.0668 Ry/atom within 6 mRy of the Barbee-Cohen result. Even for an r_s value of 1.0 (2.67 g/cm^3), denser than any of the LDA simulations reported here, we calculate only a 30-mRy difference in the total energy per atom between values of r_c of 0.3 and 1.4. Finally, for an r_c of 1.4 bohrs, the total energies at r_s^0 differ by less than 1 mRy between E_{cut} of 36 and 64 Ry. We find similar results for the other lattices.

In addition, we have tested the sensitivity of the forces to the plane-wave cutoff, E_{cut}. Since the MD simulations operate on the forces rather than the total energy, such an examination represents a more strenuous test of the parametric choices. We select as a representative case a pure H system of 54 atoms at a density of 1 g/cm^3 and a temperature of 1 eV with an r_c of 1.4 bohrs for a trajectory of 1000 time steps. At every 10 time steps, we compare the average force on each atom within the configuration calculated with E_{cut} of 36 and 64 Ry. We find a maximum difference of 2% for any time step. This maximum error occurs usually for only one atom in a configuration at a given time step with the forces on the other members given more accurately. In addition, we encounter this extreme error only a few times during the simulation. We find similar results for other temperature and density cases under investigation. Such small errors in the force guarantee a well-behaved propagation of the particles in response to the applied field. Given these findings, we typically choose for our simulations reported in the next sections (unless otherwise noted), an r_c of 1.4 bohrs for which a E_{cut} of 36 Ry gives excellent convergence.

We note one final numerical problem encountered in studying systems at elevated temperatures. For very low T_i, only those eigenvalues up to the Fermi energy become occupied. Thus, extraction of only a few roots ($= N_e/2$) from the diagonalization procedure proves necessary. However, as the temperature increases, more and more eigenstates become populated due to the FD distribution [Eq. (15)]. These states are required for an accurate description of the Mermin functional and the force as in Eq. (11). Unfortunately, iterative eigenschemes do not scale linearly as the number of roots required. Higher roots place a larger computational burden on the techniques. To represent the force to better than 1% accuracy, the highest level included in Eq. (9) should have a population of less than 10^{-4}. We have also found that this choice of occupancy cutoff enhances the convergence of the self-consistent field (SCF) step. An often encountered problem with the LDA occurs for nearly degenerate levels lying close to the occupancy cutoff. If only some of these levels are included, then poor convergence can result due to the oscillations between occupied levels at successive iterations. When all states within the degenerate group are included, the SCF converges rapidly. This empirically determined cutoff in our case guarantees that all important levels are included. Typically, to fulfill this criterion necessitates the calculation of between 70 and 120 eigenvalues for systems of 50–100 electrons at temperatures ranging from 1 to 5 eV. Therefore, differences in computational times between high- and low-temperature simulations can greatly exceed the simple ratio between the number of roots needed.

TABLE I. Total energy per atom as a function of r_s for H in bcc lattice in the LDA approximation with r_c=0.3 bohr, 145 k-point sample, and E_{cut}=36 Ry. The value from Ref. [50] is -1.0605 Ry/atom at 1.675 bohrs.

r_s (bohrs)	E_{tot}/atom (Ry)
1.626	-1.0598
1.675	-1.0606
1.724	-1.0604

2. Average properties

For the isokinetic ensemble, the total-energy fluctuates with time much as the temperature in the microcanonical picture. From this fluctuation, we can gain insights into the statistical and numerical accuracies of the simulation. As a test of the choice of parameters in the velocity Verlet propagation scheme, we determine the number of time steps in a cycle of the oscillations of the total energy E by dividing the trajectory length by the number of crossings of the mean value. For our LDA simulations, we find generally between 15 and 20 points in a cycle, sufficient to represent accurately the fluctuations [52]. The TBss' and the Moliere have closer to 50–60 points/cycle. We have also performed an analysis suggested by Friedberg and Cameron [53,30] for determining the run variance $[\sigma(\langle E\rangle_{\text{run}})]$ in the mean of the total energy. We have estimated the "statistical inefficiencies" and obtained errors in $\langle E\rangle$ of much less than 1%. For example, an LDA simulation of 54 H atoms at T = 3 eV and ρ=1.5 g/cm^3 for 1500 time steps (Δt =0.36 fs) yields a mean energy of -46.27 Ry with a run variance (error) of ± 0.1 Ry. Any drift in the average quantities lies within this variance, indicating a stable, accurate propagation over the entire trajectory length. As a further test of the basic procedures, we ran several representative microcanonical LDA simulations. As with the Li [50], we obtained energy conservation to within four significant figures over the entire trajectory. We find similar behavior for other densities and temperatures. Again, since the TBss' and

Moliere simulations employ smaller temporal steps and larger samples, the variances reach smaller values.

3. Autocorrelation functions

We take the diffusion coefficient as a representative property to illustrate the trajectory analysis. A hydrogen simulation begins with a configuration of atoms in a high-symmetry state such as bcc. The system then evolves in time according to the particle interactions in an isokinetic ensemble with a constant T_i maintained through a simple velocity scaling scheme. Atomic collisions may lead to elastic scattering, excitation, ionization, or even bonding. This evolution produces a trajectory, which contains the positions, velocities, and forces at each time step. In order to determine the autocorrelation functions in Eqs. (4), we must perform particle and time averages. The particle averages pertain at each time step; the time averages accrue over the entire length of the trajectory. However, we generally accumulate the time averages only for a series of contiguous subsets of the total trajectory. For example, the trajectory has n_t total time steps and contains averages over blocks of $n_{\rm sam}$ steps ($n_{\rm sam} \leq n_t$). In addition, the time origins at which sampling begins are usually not statistically independent, especially if they lie close together. Separating the origins by a correlation time ($n_{\rm cor}\Delta t$), which generally corresponds to the e-folding of the velocity autocorrelation function, overcomes this limitation. In Fig. 1, we present the velocity autocorrelation function $Z(t)$ for a sample of 54 H atoms at T_i of 3 eV and a density of 1.5 g/cm^3 in the DF-LDA ($L = 7.389$ bohrs) for a trajectory of 1500 time steps (Δt=0.37 fs). We note the precipitous drop at small times, followed by a long-time oscillation about zero. The correlation time of 16 steps or 5.8 fs results from determining the e-folding of $Z(t)$. The temporal integral of $Z(t)$ yields the diffusion coefficient. An estimate of the error in the diffusion coefficient [30] arises from a simple formula $[n_{\rm cor}/N_a n_t]^{\frac{1}{2}}$. For this simulation, an error of about 2% results. We can pursue this analysis further by considering the mean-square displacement (MSD) autocorrelation function as given in Fig. 2 for $n_{\rm sam}$=400 and $n_{\rm cor}$=20. At small times, the curve exhibits the quadratic temporal behavior associated with a perturbative expansion of the Einstein relationship. For longer times, a characteristic linear form emerges, denoting a diffusing fluid. The diffusion coefficient comes simply from the slope of the MSD as given by Eq. (4). In the long-time region, we invoke a linear least-squares fit to the MSD and obtain a departure from linearity of less than 2% for variations in the sample and correlation times, consistent with the findings from the velocity autocorrelation function. This result dictates a lower bound on the statistical errors in the autocorrelation functions. Similar findings hold for other densities and temperatures for LDA runs with smaller variances found for the TB and Moliere potentials. In addition, the two methods for calculating D_s afford excellent opportunities for cross comparisons of accuracy.

We regularly employ two other quantities, the pair correlation function and the translational order parameter, to describe the dense media. The translational-order parameter (TOP) displays certain behavior for different phases. For a solid, the TOP remains at a value of near unity while for a liquid, the quantity hovers around zero. Therefore, examination of the TOP ensures that the medium has actually attained a fluid state. In Fig. 3, we display the TOP for the H system discussed above. The TOP begins at unity, indicating the initial bcc (solid) configuration, and rapidly descends to the fluid state [$\rho(k,t) \approx 0$]. While determination of $g(r)$ occurs at each time step, we generally average the quantity over that portion of the trajectory beyond the onset of the fluid state. The averaging, while producing a smooth $g(r)$, masks transient structural features.

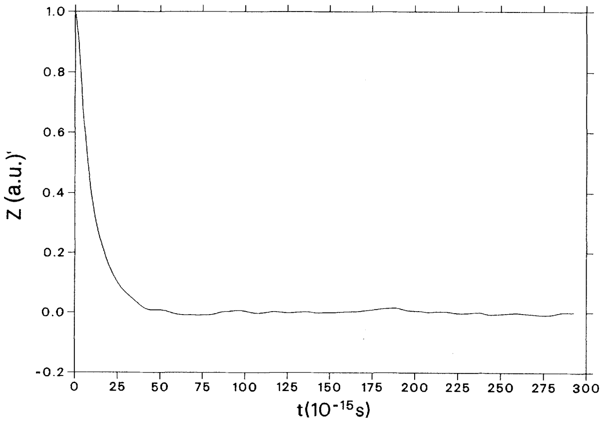

FIG. 1. Velocity autocorrelation function $Z(t)$ as a function of time for pure H at 3 eV and 1.5 g/cm^3 in the LDA with N_a=54.

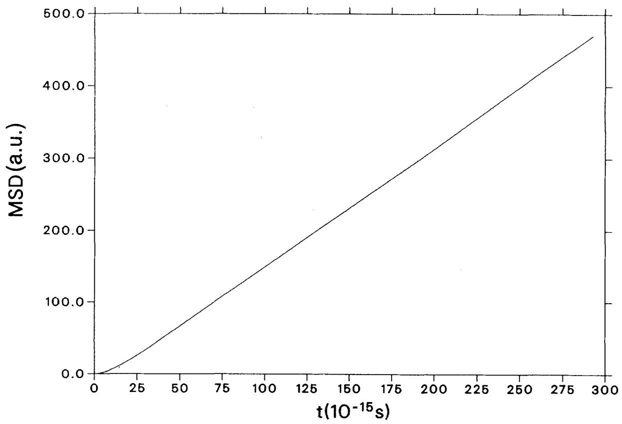

FIG. 2. Mean-square displacement as a function of time for same parameters as in Fig. 1.

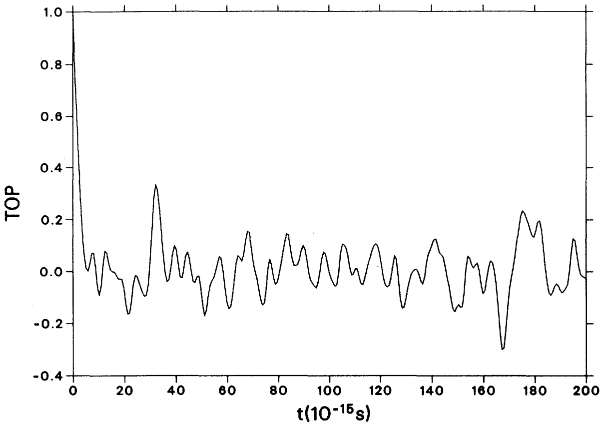

FIG. 3. Translational order parameter as a function of time with same parameters of Fig. 1.

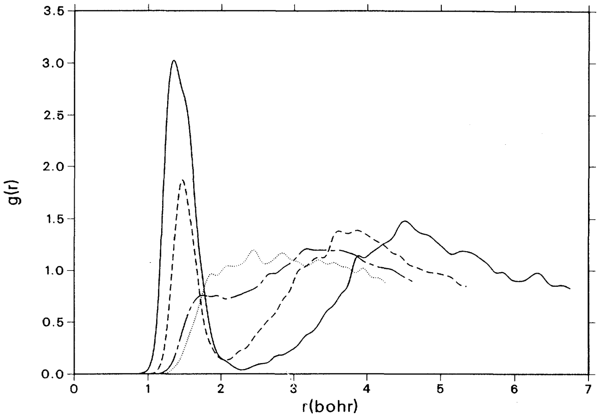

FIG. 4. Pair correlation function $g(r)$ as a function of distance r at $T = 0.1$ eV and four densities: 0.25 (solid line), 0.50 (dashed line), 0.75 (dashed-dotted line), 1.00 (dotted line) g/cm^3 in the LDA for pure H with N_a=54.

In the above section, we have estimated various statistical variances or errors for representative LDA simulations. While these remain below the general statistical sampling error of $1/\sqrt{N}$, which for a 54-atom sample gives 14%, the systematic sources of error probably rank higher. These sources include such features as the model employed, the temporal propagation, and the sample size. We have, as detailed above, gone to great lengths to ensure the proper convergence in a variety of parameters for the LDA and model interaction potentials. We have also shown stable, accurate propagation through the choice of parameters in the velocity Verlet. Finally, size effects usually arise at the order of $1/N$, which is similar to our lower statistical bounds. Probably the main source of systematic error rests with the use of the LDA approximation in the density functional scheme. While quantitative comparisons lie outside the scope of this paper (relying on more sophisticated nonlocal DF approaches), agreement between LDA calculations and experimental results for the diatomic and bulk properties indicate that the LDA provides a reasonable representation for H at the temperatures and densities under consideration. With the analysis techniques well defined, we consider both pure and mixed isotopic states of dense hydrogen.

C. Pure hydrogen: Low-temperature comparisons

We begin by investigating pure hydrogen at low temperatures and high compressions. This regime provides not only insights into the physical behavior of this system but also grounds for comparing the various techniques and models described in the previous section. In addition, while preliminary results at certain T and ρ values appeared in earlier papers, the present calculations mark longer trajectories and better sampling analysis and thus provide better cases for comparisons. Figure 4 displays the pair correlation function $g(r)$ at a temperature of 0.1 eV (1160 K) as a function of density for trajectories on the order of 1000 time steps (Δt=0.73 fs) for a 54-atom reference cell in the DF-LDA. At the lowest density, the distinctive peak of molecular hydrogen (H_2) looms prominently about its equilibrium position of 1.4 bohrs. This characterizes the medium as a molecular fluid, which corresponds to the correct physically observed phase at this density and temperature [1]. As the density increases, the molecular peak declines, indicating less relative concentration of H_2. Finally, around 1 g/cm^3, no molecular character remains, and the media become atomic. Since the temperature remains very low, the transformation from molecular to atomic fluid occurs through the pressure dissociation of the H_2 bonds by the ever closer proximity of surrounding particles. The exact transition to atomic hydrogen remains uncertain and a cynosure in the literature of hydrogen under pressure, although a value of around 1 g/cm^3 appears consistent with other studies. To accurately depict this phase change requires inclusion of the zero-point motion of the nuclei (~ 0.25 eV). However, since our interest in this low-temperature regime lies in only a general description and a comparison with methods of comparable detail, we omit this component for this study. The basic behavior of compressed hydrogen in this low-temperature regime agrees closely with comparable investigations by Younger [21] using Hartree-Fock, by Theilhaber [22] using a time-dependent DF, and by Hohl and co-workers [23] using a Car-Parrinello approach [54]. For example, at $T = 0.25$ eV (~ 3000 K) and a density of 0.50 g/cm^3 (r_s=1.75), we observe two peaks in the $g(r)$: a narrow one near the equilibrium internuclear separation (R_{eq}=1.45 bohrs) for H_2 and a broad one around 3.8 bohrs, in basic agreement with Hohl *et al.* [23]. We similarly find the first peak shifted by a small amount (0.03 bohr) from R_{eq}, slightly asymmetric, and about a factor of 1.5 higher than the second feature. At higher densities and temperatures [ρ=0.75 g/cm^3, $T = 0.75$ eV; r_s=1.5, 1500 K], our $g(r)$ exhibits the same behavior as that of Ref. [23] with the H_2 peak almost merged with the broad feature (see Fig. 4). Finally, both sets of calculations show the complete plasma character of the media at a density of 1 g/cm^3 (r_s=1.38) for T = 1200 K (0.1 eV) with a single feature having a maximum around 2.5 bohrs. Their estimate of a diffusion coefficient of order 10^{-3} cm^2/s is also in accord with our findings. Theilhaber [22] at this density and a temperature of T = 2000 K also reports a plasma state based on the form of the $g(r)$. These general trends from molecular liquid to atomic plasma also pertain in the study of Younger [21]. In addition, generally good agreement between path integral Monte Carlo and DF-LDA results for thermodynamic properties and pair correlation functions for hydrogen was found by Pierleoni *et al.* [28] for the region in a plot of T as a function of ρ below a straight line defined by T between 5 and 70 eV and ρ between 0.33 and 16.67 g/cm^3. All of the present simulations for T of 1 eV and above are safely in the agreement region of this plot.

We also present simulations with the tight-binding model that employs two s-type functions at each center. As shown in Fig. 5, the TBss' pair correlation function closely resembles the trend for the DF-LDA. The results pertain for a MD trajectory with 432 atoms of 1000 time steps (Δt=0.2 fs) after an equilibration of 5000 steps. The model supports the molecular binding into H_2 as well as the pressure dissociation at high compressions. This dissociation occurs at a slightly higher density of 1.2 g/cm^3. In general, the TB method provides reasonable results at a far less computational cost. For example, on a Cray-YMP computer a sample of 54 atoms at 1 eV and a density of 1 g/cm^3 takes on average 200 s per time step for 70 roots in the LDA and only 0.3 s for the TBss'.

Related closely to the pair correlation function by a Fourier transform, the structure factor $S(k)$ represents an experimentally measurable quantity through x-ray diffraction. For the TBss' model, we present in Fig. 6 the structure factor as a function of density for a T_i of 0.5 eV (5800 K). Not surprisingly, we note a behavior very similar to the corresponding $g(r)$. At low density, the H_2 peak dominates the k regime between 0.5 and 2 a.u. As the density rises, the molecular state gradually changes to pure atomic. The region near $k = 0$ depends strongly on the long-range radial behavior of $g(r)$. Since we confine the simulations to a reference cell of length L, the pair correlation function remains accurate only out to $L/2$. Therefore, to calculate the small-k behavior, we would have to extend the $g(r)$ by some analytical means or increase the cell size. However, the trends displayed for $S(k)$ elucidate the general features of this function without this extension.

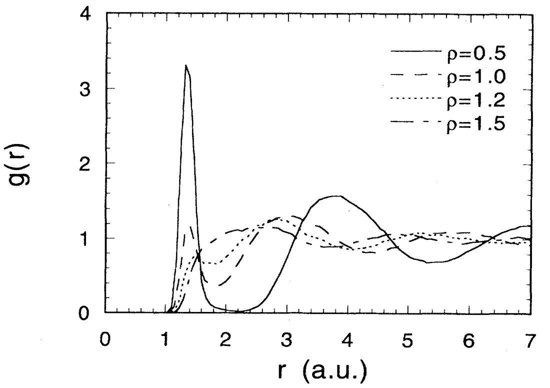

FIG. 5. Pair correlation function at T = 0.1 eV for four densities: 0.50 (solid line), 1.00 (dashed line), 1.25 (dotted line), and 1.50 (dashed-dotted line) g/cm^3 in the TBss' model for pure H with N_a=432.

D. Pure hydrogen: High temperature

We now fix the density and follow the system through a series of temperature increases. Figure 7 shows such

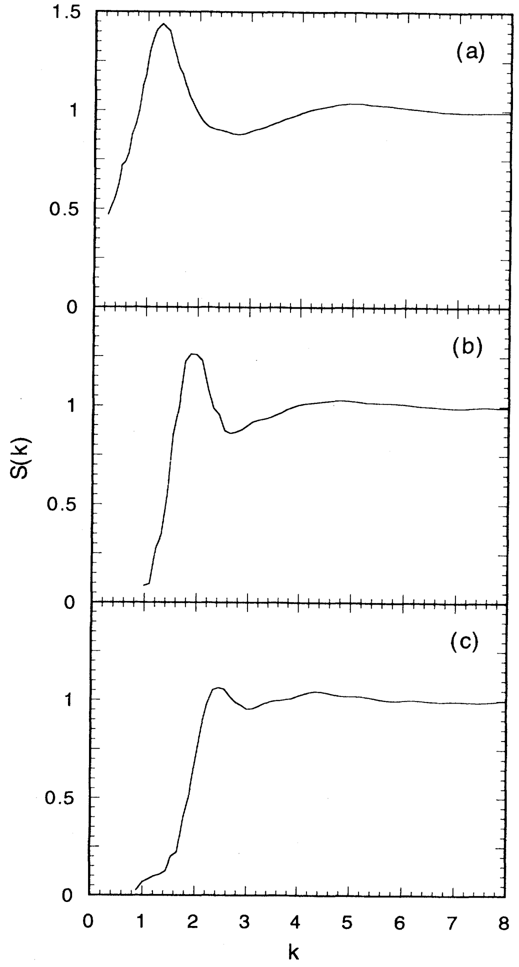

FIG. 6. Static structure factor $S(k)$ for the TBss' model at T = 0.5 eV for three densities: (a) 0.1, (b) 0.5, and (c) 1 g/cm^3 with k in a.u.

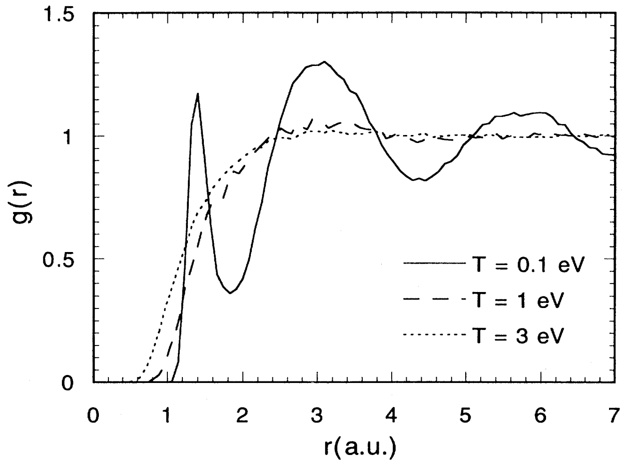

FIG. 7. The pair correlation function $g(r)$ for the TBss' model at ρ=0.5 g/cm^3 for three temperatures (T_i): 0.1 eV (solid line), 1 eV (dashed line), and 3 eV (dashed-dotted line).

a tract in terms of the pair correlation function $g(r)$ for H at a density of 0.5 g/cm^3 in the TBss' for 432 atoms. We present three ionic temperatures of 0.1, 1, and 3 eV, which correspond to classical coupling constant (Γ) values of 155, 16, and 5, respectively. At low temperature the molecular fluid pertains. However, as T_i rises, the H_2 peak disappears much as in the case of rising pressure. At the highest temperature, the fluid has reached a completely atomic phase as indicated by the featureless pair correlation function. The hydrogen bonds break due to fast collisions between the constituent particles.

We have so far concentrated on the general structure of the fluid since the pair correlation function incorporates a time average over the trajectory. However, such averaged quantities may miss transient features of the system evolution. For example, recent MD-LDA calculations [23,55] on dense hydrogen at low temperatures have discovered long chains of molecules that form, dissolve, and reform over the course of the simulation. A poignant example of such time-dependent processes at higher temperatures appears in Fig. 8, which displays contour plots of the electron density in a plane through the reference cell for H at 3 eV and 1.5 g/cm^3 at several time steps. While properties such as diffusion might at a certain T_i become comparable to the OCP values, the actual charge density shows a significant departure from the expected uniform OCP background for the electrons. Groups of atoms coalesce, resulting in charge densities many times the simple addition of unperturbed atomic charge distributions. Such departures indicate strong interaction among the particles. At this temperature, the events are transient so that no permanent molecular bonds form. However, for many MD cycles, groups of atoms remain in close contact. Such collections of atoms can have profound effects on the radiative and, to a lesser extent, the transport properties of dense systems.

We now consider these associations of atoms in more detail, particularly concentrating on structures that maintain close proximity for reasonably long times. For a representative case, we choose an LDA simulation of 800 time steps [Δt=0.73 fs] for 54 atoms at T = 1 eV and ρ=1.0 g/cm^3 and investigate the behavior of the interatomic separation r_{ij} (= $|\mathbf{r}_i - \mathbf{r}_j|$) of various pairs of atoms over time. At this density, the bcc structure yields a nearest-neighbor distance $R_{\rm NN}$ of 2.44 bohrs. In Fig. 9, we present this function for atoms 39 and 47 over a part of the trajectory. We note that for a time frame of over

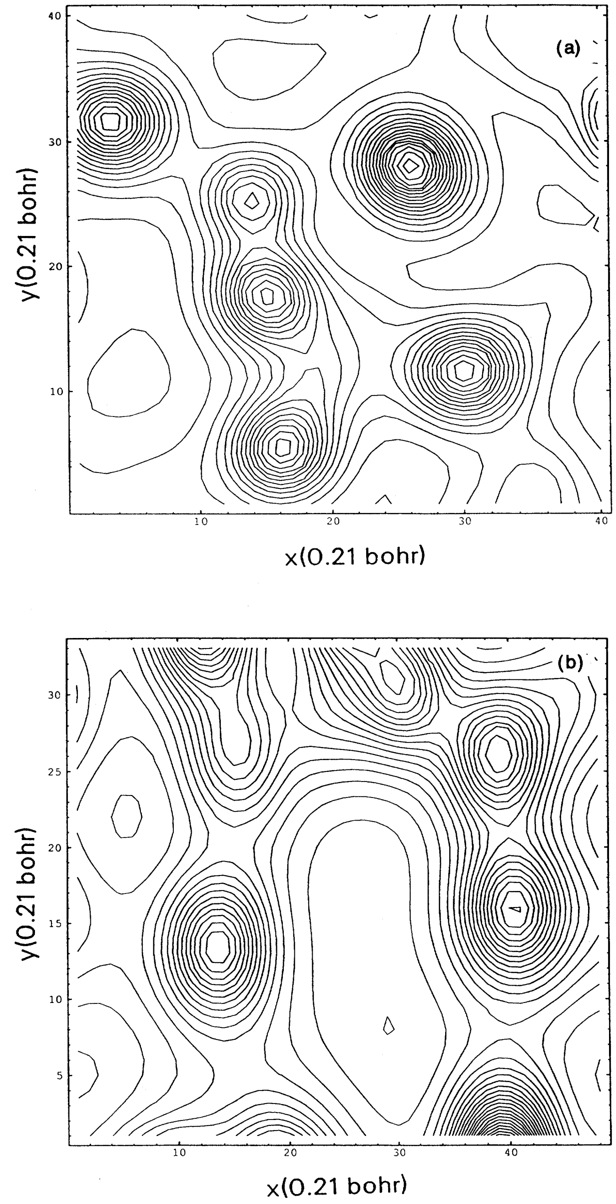

FIG. 8. Charge density contours in the xy plane in the LDA for T = 3 eV and ρ=1.5 g/cm^3 at two different time steps: (a) 390 and (b) 1290 of the trajectory. Axes scale: 1 unit = 0.21 bohr.

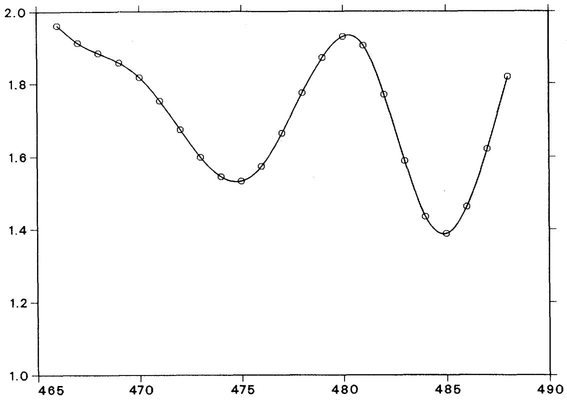

FIG. 9. Interatomic separation r_{ij} (bohr) as a function of time for atoms 39 and 47 in an LDA H simulation of 54 atoms at $T = 1$ eV and ρ=1 g/cm^3.

18 fs the pair remain at a distance less than 2.0 bohrs. In addition, r_{ij} oscillates around the value of ~ 1.75 bohrs for a "period" of about 10-fs duration. This time is of the same order as the vibrational period of H_2 in its electronic ground state (7.3 fs). We find that such associations, in which two atoms remain closer than 2.0 bohrs for more than 10 time steps (7 fs), occur for over 20% of the pairs. Several such clusterings arise for each pair during the duration of the trajectory (about 10–15% of the time). Therefore, at any time step along the trajectory, between 1% and 5% of the *pairs* are undergoing a long-time association. Thus, this clustering is not a rare event and may have profound ramifications on the radiative properties of the media [56]. We have also found multiple associations ($N \geq 3$) that last for tens of femtoseconds although these remain much rarer. Figure 10 presents the r_{ij} values for three atoms 24, 25, and 34 from an LDA simulation of 54 H atoms at $T = 3$ eV and ρ=1.5 g/cm^3 for 1500 time steps [Δt=0.37 fs, $R_{\rm NN}$=2.13 bohrs]. We note a close association of all three nuclei for a period of over 10 fs. In addition, atoms 24 and 34 (triangles) remain in close contact for over 20 fs and perform two full oscillations about 1.75 bohrs. Figure 11 further illustrates this result by presenting three-dimensional (3D) snapshots of this encounter at selected time steps corresponding to Fig. 10. For display purposes, each frame has been rotated into the plane of the three atoms, and the "bonds" drawn for better visual perspective. The pair (24,34), marked by triangles in the previous figure, appear at the top of each frame. We observe atom 25 approach, form a close association with the other two, and then depart. This more graphically represents the spatial encounter depicted in Fig. 10 and serves to illustrate these temporal groupings or clustering. We find similar groupings for other densities [0.5 ≤ ρ ≤ 2 g/cm^3] and temperatures [1 ≤ T_i ≤ 5 eV]. Such effects also occur in the TB*ss'* model but with somewhat less frequency. This may indicate that higher excited states are needed to properly model the surface for intermediate-energy collisions.

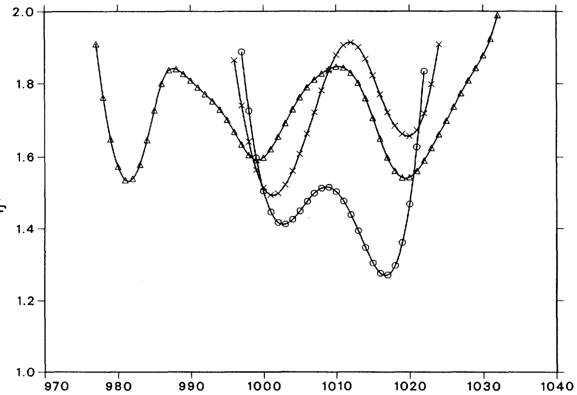

FIG. 10. Same as Fig. 9 except for three atoms (24, 25, and 35) at $T = 3$ eV and ρ=1.5 g/cm^3. Pair designations: (24,25), circle; (24,34), triangle; and (25,34), cross.

The question now arises as to the physical nature of these temporal associations. The basic behavior of two atoms approaching, oscillating about each other for a short time, and departing mimics the expected effects in collisions marked by a shape or barrier-trapping resonance. The energy involved in the collisions studied ($E < 5$ eV) lies well below the excitation threshold for the excited states of atomic hydrogen. However, for simple H+H collisions, the combination of an attractive ground-state potential with the centrifugal barrier produces a curve that effectively traps the atoms at short distances for a finite time. Since the particles start in the continuum, they must by conservation of energy, end there, making the trapping a temporary phenomenon. For the H+H system [57], the resonances have typical lifetimes of 50–100 fs, somewhat longer than observed in the above simulations. However, the actual situation becomes complicated by the presence of the surrounding H atoms. The interaction of these atoms with the collisional pair dis-

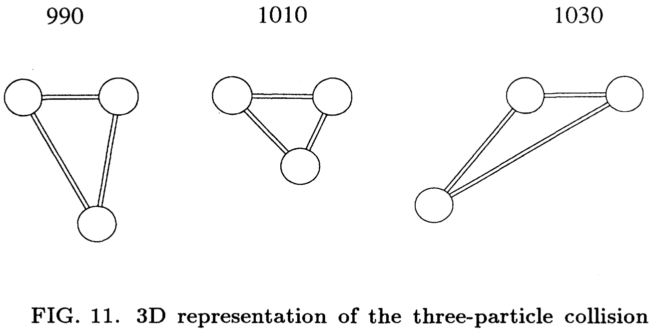

FIG. 11. 3D representation of the three-particle collision displayed in Fig. 10 for time steps 990, 1010, and 1030. Each frame rotated into plane of the three atoms. Top pair represents atoms 24 (left) and 34 (right); atom 25 collides from below.

torts the simple two-body potential such as the collinear reaction barrier [58] in H_3. Therefore, the actual situation is complicated, having contributions from a complex many-body electronic surface and centripetal terms. The resonances so far described arise from a full quantum mechanical treatment of the TD Schrödinger equation, and would not strictly appear in the classical solutions of Eq. (1) for the nuclear motion. However, the changing topography of the interaction surface with time provides ample opportunities for trapping a few particles within a barrier. These particles would closely interact until this barrier finally weakened or disappeared from changes in the surface due to the surrounding particles. The behavior would closely resemble a true shape resonance. Therefore, the basic concept of such barrier-trapping resonances appears to have merit in describing these H collisions. No matter what the trapping mechanism, such long-lived associations will yield highly distorted charge distributions among its constituents.

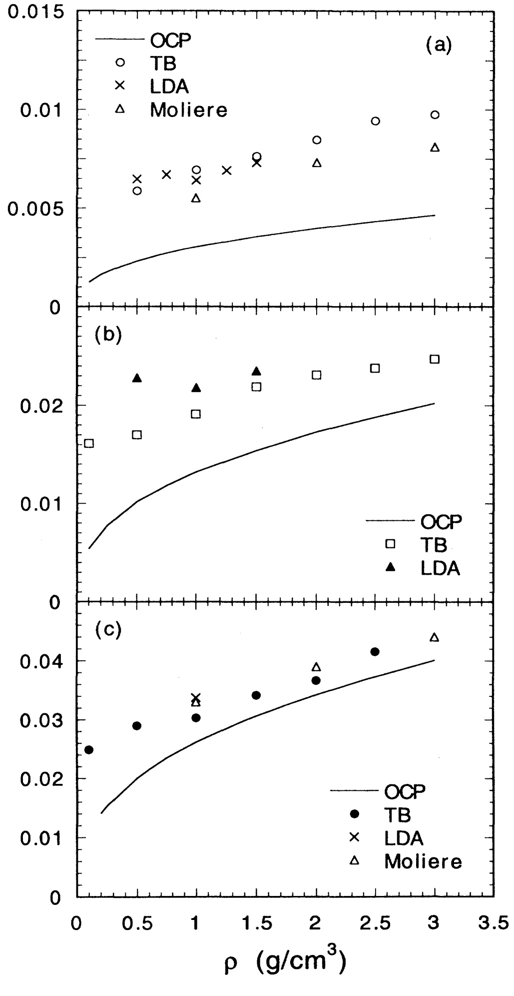

FIG. 12. Comparison of density times the diffusion coefficient (ρD) as a function of density for pure H at three temperatures: (a) 1, (b) 3, and (c) 5 eV for four different methods: LDA (cross, triangle), TB*ss*′ (circle, square), Moliere (open triangle), and OCP (line).

Having elucidated some structural aspects of the dense media, we turn to a discussion of the dynamical properties as represented by the diffusion coefficient, D_s. While analysis of the trajectory provides various other properties such as viscosity and thermal conductivity, we shall focus on diffusion since convergence comes for moderately short trajectories, particle averages reduce statistical errors, and the long-time tail behavior presents little difficulty [30]. In Fig. 12, we compare the self-diffusion coefficients (ρD), as a function of density and temperature for four interaction models: DF-LDA, TB*ss*′, Moliere, and the classical OCP [15]. At the lowest temperature (1 eV), the DF-LDA and TB*ss*′ models agree very well over a range of densities. However, the OCP remains almost a factor of 4 too low. The classical coupling constant Γ ranges from 15 to 28 for the density range 0.5 to 3.0 g/cm^3. While this corresponds to the strongly coupled regime, the quantum mechanical effects prevail since the ions remain highly screened. As T_i increases, the agreement between the TB and LDA continues very good, and the OCP comes into better accord. At the higher temperatures, the media become reasonably ionized, and the electronic wave function spreads over many sites. This gives the appearance of point ions within a uniform charge background—the physical model of the OCP. However, even for 5 eV in which Γ ranges from 3.1 to 5.7, the TB and LDA diffusion coefficients exceed the OCP by 30%. In addition, the Moliere pure pair potential results show good agreement with the more sophisticated models over a considerable range of density and temperature. However, this model contains no explicit representation of the electronic component and therefore, will not give the proper low-temperature behavior such as molecular binding nor yield radiative or electronic properties such as ac and dc conductivities. A closer examination of the Moliere model in Fig. 13 demonstrates that its pair correlation function displays apparent differences

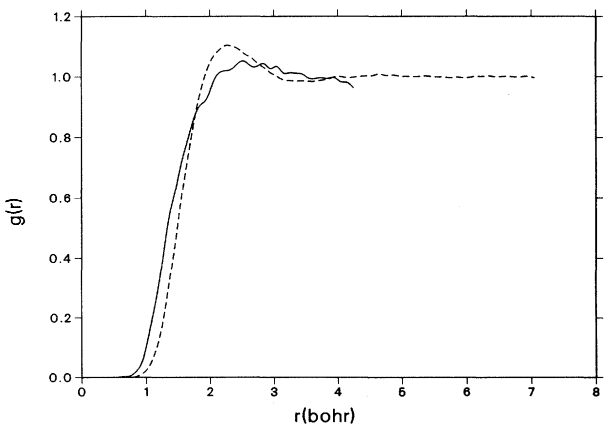

FIG. 13. Pair correlation function $g(r)$ at $T = 1$ eV and ρ=1 g/cm^3 for the Moliere (dashed line) and LDA (solid line).

TABLE II. Comparison of the density times the self-diffusion coefficients for pure H as a function of density for several models at three temperatures. Numbers in brackets signify powers of 10.

ρ (g/cm^3)	ρD [g/(cm s)]		
	LDA	TB	Moliere
		$T = 1$ eV	
0.5	6.5[−3]	5.9[−3]	
1.0	6.4[−3]	6.9[−3]	5.5[−3]
1.5	7.3[−3]	7.6[−3]	
2.0		8.5[−3]	7.3[−3]
3.0		9.7[−3]	8.1[−3]
		$T = 3$ eV	
0.5	2.3[−2]	1.7[−2]	
1.0	2.4[−2]	1.9[−2]	1.8[−2]
1.5	2.3[−2]	2.2[−2]	2.1[−2]
2.0		2.3[−2]	2.2[−2]
3.0		2.5[−2]	2.5[−2]
		$T = 5$ eV	
0.5		2.9[−2]	
1.0	3.2[−2]	3.0[−2]	3.3[−2]
2.0		3.7[−2]	3.9[−2]

from the LDA. The LDA shows a deeper penetration and therefore "softer" potential. Also, the characteristic bump in the Moliere near 1.8 bohrs does not appear in the LDA result. Table II summarizes the results given in Fig. 12. Finally, we compare with the Thomas-Fermi DF calculations [24] at a density of 2.5 g/cm^3. At a temperature of 0.5 eV [$\Gamma \approx 50$], the TBss' gives a diffusion coefficient a factor of 2 larger. However, at the higher T_i (=2.5 eV, $\Gamma \approx 10$), the two techniques agree to within 11%. Over a broad range of Γ, indicative of a strongly coupled regime, the diffusion coefficient depends more on quantal rather than classical effects.

E. Isotopic mixtures

We shall display results for several different hydrogenic isotopic species: hydrogen (H, 1 amu), deuterium (D, 2 amu), and tritium (T, 3 amu) at several representative densities and temperatures. In addition, we restrict the presentation to equimolar concentrations ($N_1 = N_2$) of binary mixtures and report only the total molar density, [n (mole/cm^3)] = 11.206 (n_1+n_2) with $n_i = N_i/L^3$. All calculations employed the isokinetic ensemble in which the temperature remains constant at T_i due to velocity scaling. In an earlier work [59], we focused primarily on the HT system. Here, we expand our presentation to include all three permutations [HT, DT, and HD]. The differences in behavior among the various mixtures play important roles in many macroscopic processes, for example, in the optimal choice of fuel in ICF capsules. Therefore, presenting but one mixture, for example HT, leaves an incomplete picture of the isotopic behavior.

Before discussing the mixtures in detail, we first explore some basic features of pure isotopic systems that bear particular relevance to the composites. For a single-species fluid, the mass becomes merely a scaling parameter in the equations of motion [Eq. (1)]. The usual treatment employs scaled variables in which the new time incorporates the square root of the mass. The electronic potential energy, and therefore the force, remain the same for all the isotopes since these quantities have no mass dependence. Therefore, the same scaled equation of motion fits all isotopes. To obtain the dynamical evolution of the systems for all three isotopes requires only the solution of one scaled equation. However, to extract the actual property in common units (cgs) necessitates a transformation. For the self-diffusion coefficient that has units of length^2/time, the actual quantity is proportional to the scaled value over $\sqrt{m_i}$. Therefore, for pure isotope species i and j, the following relationship holds:

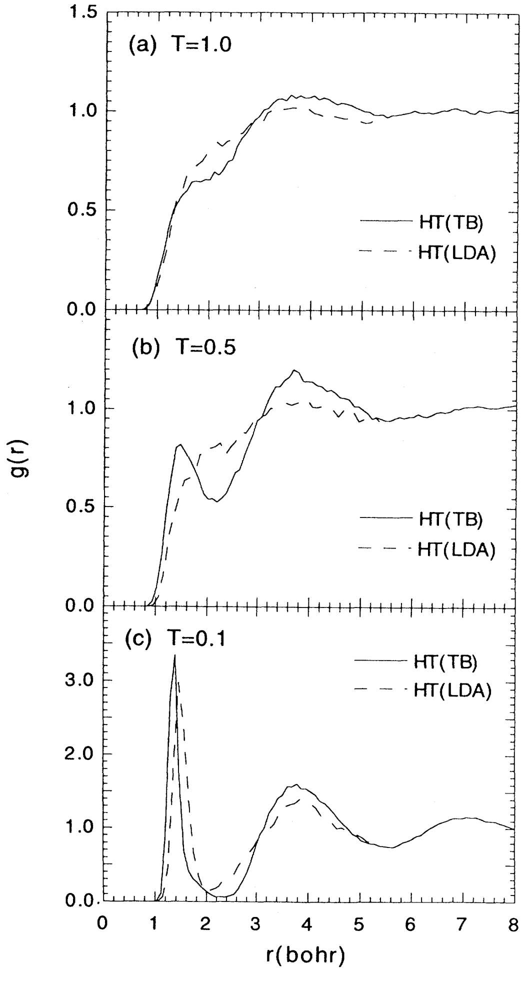

FIG. 14. Pair correlation functions for HT equimolar mixture in the DF-LDA and TBss' models at 0.5 moles/cm^3 at three temperatures: (a) 1.0, (b) 0.5, and (c) 0.1 eV for $g_{\rm HT}$: DF-LDA (dashed line) and TBss' (solid line).

$$\frac{D_i}{D_j} = \sqrt{\frac{m_j}{m_i}}, \tag{19}$$

which yields 0.577, 0.816, and 0.707 for $D_{\rm T}/D_{\rm H}$, $D_{\rm T}/D_{\rm D}$, and $D_{\rm D}/D_{\rm H}$, respectively. We would also obtain these ratios for a mixture with intraspecies interactions but not interspecies connections. In fact, the self-diffusion coefficients for pure D and T follow directly from Eq. (19) using the results for H from the previous section. Reversing this prescription provides an excellent test of the MD simulation programs for mass explicitly included, a necessary modification to treat mixtures. We have performed calculations with both the TB*ss'* and Moliere models with the mass included in Eq. (1) and found agreement to better than a few percent with the predicted ratios of Eq. (19). However, introducing the interspecies interactions will cause departure of transport properties from the simple ratio of Eq. (19). The magnitude of this departure provides an excellent gauge of the full effects of the interplay between the two species.

TABLE III. Comparison of self-diffusion coefficients for HT mixture as a function of molar density for several models at T_i=1 eV. Numbers in brackets signify powers of 10.

n (mol/cm^3)	$D_{\rm H}$ (cm^2/s) LDA	TB	Moliere	$D_{\rm T}$ (cm^2/s) LDA	TB	Moliere
0.5	1.5[−2]	9.8[−3]	7.0[−3]	1.2[−2]	1.0[−2]	6.4[−3]
1.0	6.2[−3]	5.4[−3]	4.4[−3]	5.7[−3]	5.3[−3]	4.1[−3]
1.5	3.6[−3]	4.0[−3]	3.3[−3]	3.8[−3]	4.1[−3]	3.1[−3]
2.0		2.3[−3]			2.2[−3]	

We begin our discussion of the basic structural behavior of these mixtures by examining the pair-correlation functions. Figure 14 presents a comparison for the cross-pair correlation function $g_{\rm HT}(r)$ between the DF-LDA and TB*ss'* cases for an HT mixture at 0.50 mol/cm^3 at several temperatures (Γ= 15–155). The TB*ss'* model employed a sample of 250 atoms (125 H, 125 T) while the LDA utilized only 54, which corresponds in each case to a total number density of 4.46 × 10^{-2} particles/bohr^3. For the LDA (TB*ss'*), the trajectories were accumulated over 1000 time steps (n_t) in increments of Δt = 0.73

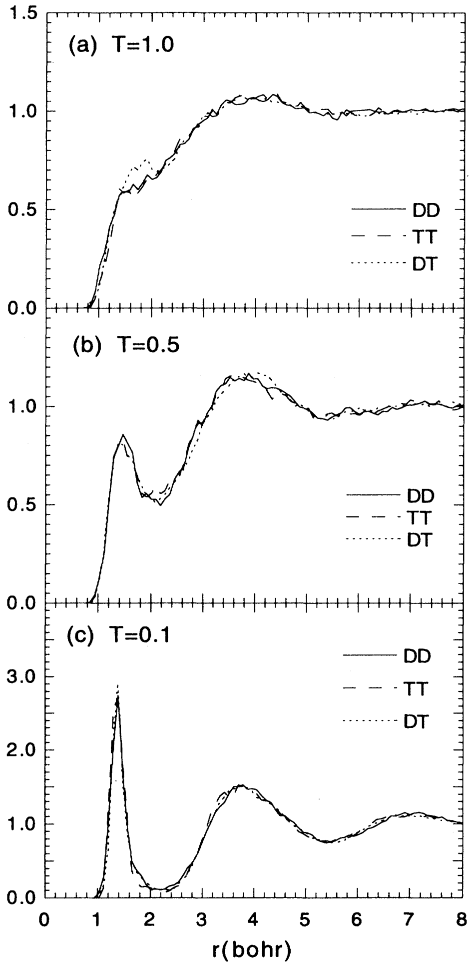

FIG. 15. Pair correlation functions for DT equimolar mixture in the TB*ss'* model at 0.5 moles/cm^3 at three temperatures: (a) 1.0, (b) 0.5, and (c) 0.1 eV for $g_{\rm DD}$ (solid line), $g_{\rm TT}$ (dashed line), and $g_{\rm DT}$ (dotted line).

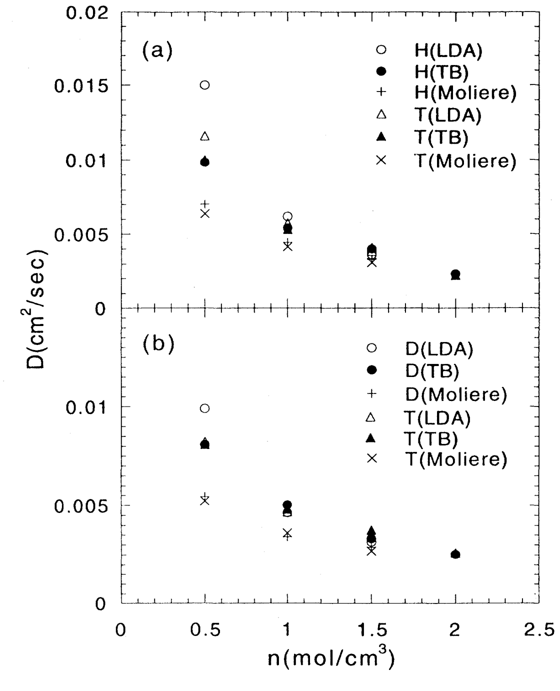

FIG. 16. Comparison of the self-diffusion coefficients of three models: LDA (open circle, triangle), TB*ss'* (closed circle, triangle), and Moliere (crosses) for T = 1 eV for two equimolar mixtures: (a) HT and (b) DT.

TABLE IV. Comparison of self-diffusion coefficients for HT mixture as a function of molar density for several models at T_i=0.5 eV. Numbers in brackets signify powers of 10.

n (mol/cm^3)	D_H (cm^2/s)		D_T (cm^2/s)	
	LDA	TB	LDA	TB
1.0	2.3[−3]	2.8[−3]	2.5[−3]	2.8[−3]
1.5	1.8[−3]	2.4[−3]	1.7[−3]	2.6[−3]
2.0		1.9[−3]		1.7[−3]

fs (0.146 fs) after an initial equilibration of 500 (5000) steps. The behavior qualitatively resembles in many aspects that of pure H (Fig. 7). At low temperatures, the mixture forms a molecular fluid signified by the distinctive peaks of the diatomic molecular isotopes H_2, T_2, and HT at their mutual equilibrium separation around 1.4 bohrs. The slight shift in the position of the lowest peak arises from the difference in the equilibrium separation predicted by the two methods. As the temperature rises, the molecular peak gradually disappears until nothing remains by 1 eV. The motion of the nuclei has become sufficient for collisions between molecules to break the hydrogen bonds. The system at this stage resembles a simple atomic fluid. The LDA and TBss' models show considerable similarity at the highest temperature. However, they differ at the transition temperature of around 0.5 eV, indicating the sensitivity of the transition to the nature of the interaction potential. The LDA, as observed for pure H, makes the transition to the atomic fluid at a slightly lower temperature. We also observe a similar difference in the transition for a fixed temperature and increasing density. This transition region remains small with good agreement at the higher temperatures and densities between the LDA and TBss' models. This same trend manifests itself in the DT mixture as indicated in Fig. 15, which displays all three pair correlation functions g_DD, g_TT, and g_DT. At the lowest temperature, we observe equal portions of the molecules since all the electronic potential surfaces at this level have the same form. Longer equilibration times generally apply in order to attain this equal distribution since the two components have different time scales. With the temperature, and therefore the kinetic energy, held fixed in the isokinetic scheme, the heavier particles travel at slower velocities. To accumulate enough collisions to obtain a balance between the association and dissociation of the molecular bonds usually requires a longer time than for the pure H system. At this temperature, the zero-point motion ($\sim$ 0.25 eV) becomes important and should be included for high precision results, but, as with pure H, we omit this contribution that lies outside the principal thrust of our study of higher temperatures.

We now investigate the dynamical properties of such mixtures through the self-diffusion coefficients (D_s) by comparing the three models: DF-LDA, TBss', and Moliere. The former, employing the most sophisticated representation of the interactions, serves as the standard by which to judge the other two approaches. We present the self-diffusion coefficients D_s for the three models at a fixed T_i = 1 eV as a function of molar density (Γ=15–24) for mixtures of HT and DT in Figs. 16(a) and 16(b), respectively. The DF-LDA, TBss', and Moliere models employed the following parameters, respectively: N_{12}=54, 250, 250; n_t=2000, 6000, 5000; and Δt = 0.725, 0.146, 0.146 fs with N_{12} defined as the total particle number (N_1 + N_2). The lowest density marks the greatest differences among the methods. Such densities correspond to atoms that interact at long and intermediate distances. For such separations the interaction potentials display considerable sensitivity to the sophistication of the model with exchange and correlation making significant contributions to the interaction surface. As the density rises, the atoms make closer contact, and the short-range part of the potential, heavily influenced by the nuclear repulsion component, plays a vital role. The more approximate models better represent this regime, and we would thus expect closer agreement as the system becomes more compact. Since the TB model has an approximate representation of these more complex quantum mechanical effects, we would anticipate agreement with the DF-LDA at a lower density. The results displayed in Fig. 16 validate these qualitative predictions. The DF-LDA and TBss' begin

TABLE V. Comparison of self-diffusion coefficients for DT mixture as a function of molar density for several models at T_i=1 eV. Numbers in brackets signify powers of 10.

n (mol/cm^3)	D_D (cm^2/s)			D_T (cm^2/s)		
	LDA	TB	Moliere	LDA	TB	Moliere
0.5	9.9[−3]	8.1[−3]	5.4[−3]	8.2[−3]	8.1[−3]	5.2[−3]
1.0	4.6[−3]	5.0[−3]	3.4[−3]	4.7[−3]	4.8[−3]	3.6[−3]
1.5	3.2[−3]	3.3[−3]	2.9[−3]	3.6[−3]	3.8[−3]	2.7[−3]
2.0		2.5[−3]			2.6[−3]	

TABLE VI. Comparison of self-diffusion coefficients for HD mixture as a function of molar density for several models at T_i=1 eV. Numbers in brackets signify powers of 10.

n (mol/cm^3)	D_H (cm^2/s) LDA	TB	Moliere	D_D (cm^2/s) LDA	TB	Moliere
0.5	1.2[−2]	1.1[−2]	7.4[−3]	1.2[−2]	1.0[−2]	7.1[−3]
1.0	6.2[−3]	7.0[−3]	4.8[−3]	5.3[−2]	6.2[−3]	4.6[−3]
1.5			3.6[−3]			3.6[−3]

to show considerable agreement by 1 mol/cm^3 and continue in accord as the molar density n increases. On the other hand, the Moliere more slowly approaches the general consensus, becoming comparable to the other two models by 1.5 mol/cm^3. This trend appears for both the HT and DT cases; we also observe similar behavior for the HD system. Since the DF-LDA case has such a few number of atoms for each species (N_i=27), we have performed calculations over sample sizes of 108 atoms for a trajectory of 2000 time steps at a few representative densities. Within the statistical error, the results closely match those for the smaller sample. In addition, we have performed calculations with up to 432 atoms for the TBss' model and 1024 atoms for the Moliere in order to establish meaningful sample levels. A more quantitative representation of the graphical data appears in Tables III–VI.

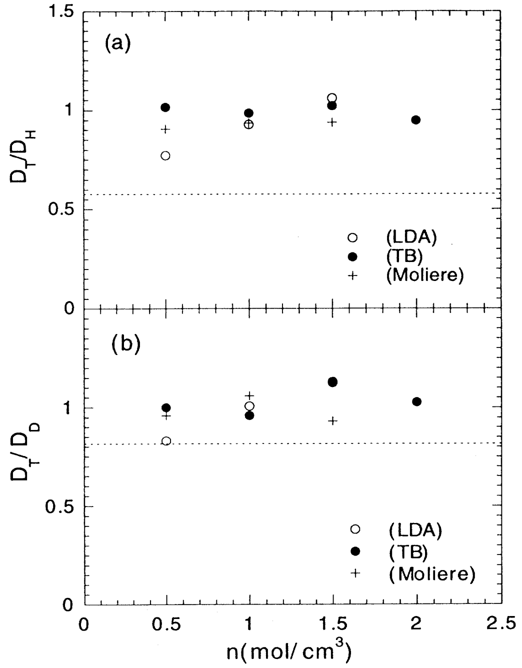

FIG. 17. Comparison of the ratio of self-diffusion coefficients for three models: LDA (open circle), TBss' (closed circle), and Moliere (cross) for T = 1 eV for two equimolar mixtures: (a) HT and (b) DT. Dashed line depicts ratio for pure species.

We also notice in Fig. 16 an interesting trend: as the density rises, the ratio of the two self-diffusion coefficients hovers around unity. This contrasts sharply with our earlier finding [Eq. (19)] for two noninteracting species that this ratio should depend on the square root of the masses. To explore this trend in more detail, we present in Fig. 17, a comparison of the ratio of the self-diffusion coefficients for the mixture (symbols) against the ratio for the pure systems (dashed line) for the three models at T_i=1 eV. For HT, the mixture ratio rests almost a factor of 2 above the pure fluids and for DT almost 25% above. This effect probably arises from the additional collisions afforded by the interspecies interactions. Corrections to simple dense gas formulas for mixtures due to collisions between different species tend to have a similar effect [34]. We also observe similar trends at other temperatures and for HD. This finding emphasizes the need for moderately sophisticated models of the full mixture in these temperature and density regimes.

To converge the mutual-diffusion coefficients requires extremely long trajectories, unfortunately out of range of any DF-LDA calculations. However, we have performed simulations of HT at 1 eV for several densities in both the TBss' and Moliere potential schemes. We begin to reach well behaved values for these quantities after about 10 000 time steps. However, for safety, we employed between 30 000 and 40 000 steps in most trajectories, longer than in our previous report [59]. For isotopic binary mixtures of nearly equal masses, the mutual diffusion coefficient D_{12} assumes a particularly simple form [32]:

$$D_{12} = x_1 D_1 + x_2 D_2, \tag{20}$$

where x_i defines the concentration (N_i/N_{12}). In many cases, this form has been shown valid well outside its derived range. We have found that for isotopic hydrogenic mixtures this form usually predicts too low a value compared to the actually calculated D_{12} although usually only by less than 25%. We present a representative example in Table VII for an HT mixture at 1 eV as a function of molar density for the TBss' and Moliere models. A similar trend holds for the Moliere potential for HD, where at n of 0.5, 1.0, and 1.5 mol/cm^3, D_{12} has values of 8.9, 6.0, and 3.1 × 10^{-3} cm^2/s, respectively. Therefore, the approximation provides moderately accurate mutual diffusion coefficients from the self-diffusion, which converges for much shorter trajectories.

TABLE VII. Mutual diffusion coefficients in units of 10^{-3} cm^2/s for HT mixture at 1 eV as a function of molar density (mol/cm^3) in the TBss' and Moliere models. $\bar{D}_{12} = \frac{1}{2}(D_1 + D_2)$.

	TBss'		Moliere	
n	D_{12}	$\bar{D}_{12}$	D_{12}	$\bar{D}_{12}$
0.50	9.6	9.0	7.0	6.7
1.00	5.9	5.6	5.2	4.2
1.50	5.1	4.2	3.9	3.2

IV. SUMMARY

We cannot hope in a short conclusion to summarize all the many findings for hot, dense hydrogen contained in the past few sections. However, a few highlights should receive emphasis. First, for pure hydrogen, basic structural and dynamical properties depend strongly on the level of treatment of the electrons. Clearly, even at the elevated temperatures, quantal effects remain important. Second, transient associations of atoms ("clusters") persist over many MD cycles. These associations, which rarely bind at temperatures greater than 1 eV, drastically alter the charge distribution around the collective sites from a simple superposition of atomic wave functions. This distortion can profoundly affect radiative properties of the media. Third, quantum mechanical simulations remain important for mixtures. The self-diffusion coefficients for the constituent species exhibit perceptible deviations from simple mass scaling rules derived from the pure species. In short, quantum molecular dynamics simulations of hydrogen in this intermediate regime between molecular liquid and a fully stripped, very hot plasma provide invaluable information on the basic nature of the medium.

ACKNOWLEDGMENTS

We gratefully acknowledge useful conversations with Dr. S. Younger, Dr. J. Erpenbeck, Dr. B. Holian, Dr. L. Pratt, and Dr. R. Martin and computer time provided under the Christmas cycles program at Los Alamos. We also wish to thank Dr. H. Brand for assistance with the graphics. This work was performed under the auspices of the U.S. Department of Energy through the Theoretical Division of the Los Alamos National Laboratory.

---

[1] H.K. Mao and R.J. Hemley, Am. Sci. **80**, 234 (1992); Rev. Mod. Phys. **66**, 671 (1994).

[2] N.W. Ashcroft, Nature **340**, 345 (1989); *Molecular Systems Under High Pressure*, edited by R. Pucci and G. Piccito (Elsevier Science, Amsterdam, 1991); E. Kaxiras, J. Broughton, and R.J. Hemley, Phys. Rev. Lett. **67**, 1138 (1991); V. Natoli, R.M. Martin, and D.M. Ceperley, Phys. Rev. Lett. **70**, 1952 (1993), and references therein.

[3] H. Iyetomi and S. Ichimaru, Phys. Rev. A **34**, 3203 (1986).

[4] S. Ichimaru, Rev. Mod. Phys. **54**, 1017 (1982).

[5] *Strongly Coupled Plasmas*, edited by F.J. Rodgers and H.E. DeWitt (Plenum, New York, 1988).

[6] *Strongly Coupled Plasma Physics*, edited by H.M. van Horn and S. Ichimaru (Rochester Press, Rochester, 1993).

[7] D. J. Stevenson, Ann. Rev. Earth Planet. Sci. **10**, 2571 (1982).

[8] G. Chabrier, N.W. Ashcroft, and H.E. DeWitt, Nature **360**, 48 (1992).

[9] J.D. Lindl, R.L. McCoy, and E.M. Campbell, Phys. Today **45**(9), 32 (1992); W.J. Hogan, R. Bangester, and G.L. Kulcinski, *ibid.* **45**(9), 42 (1992); B.G. Levi, *ibid.* **47**(9), 17 (1994), and references therein.

[10] V.D. Vikharev, S.V. Zakharov, V.P. Smirnov, A.N. Starostin, A.E. Stepanov, M.V. Fedulov, and V.Ya. Tsarfin, Zh. Eskp. Teor. Fix. **99**, 1133 (1991) [Sov. Phys. JETP **72**, 631 (1991)]; D.J. Heading, J.P. Marangos, and D.D. Burgess, J. Phys. B **25**, 4745 (1992).

[11] *Megagauss Technology and Pulse Power Applications*, edited by C.M. Fowler, R.S. Caird, and D.J. Erickson (Plenum, New York, 1987).

[12] L.A. Crum, Phys. Today **47**(9), 22 (1994).

[13] L. A. Collins, J. D. Kress, D. L. Lynch, and N. Troullier, J. Quantum Spectrosc. Radiat. Transfer **51**, 65 (1994).

[14] S.G. Brush, H.L. Sahlin, and E. Teller, J. Chem. Phys. **45**, 2102 (1966).

[15] J.-P. Hansen, Phys. Rev. A **8**, 3096 (1973); E.L. Pollock and J.-P. Hansen, *ibid.* **8**, 3110 (1973); J.-P. Hansen, G.M. Torrie, and P. Viellefosse, *ibid.* **16**, 2153 (1977).

[16] D. Liberman, Phys. Rev. B **20**, 4981 (1979).

[17] C. Dharma-wardana, in *Strongly Coupled Plasma Physics*, edited by F.J. Rogers and H.E. Dewitt (Plenum, New York, 1988), p. 275; M.W.C. Dharma-wardana and F. Perrot, Phys. Rev. A **26**, 2096 (1982); F. Nardin, G. Jacucci, and M.W.C. Dharma-wardana, *ibid.* **37**, 1025 (1988).

[18] L.A. Collins and A. Merts, in *Radiative Properties of Hot Dense Matter*, edited by J. Davis, C. Hooper, R. Lee, A. Merts, and B. Rozsnyai (World Scientific, Singapore, 1985), p. 385.

[19] S.M. Younger, A.K. Harrison, and G. Sujigama, Phys. Rev. A **40**, 5256 (1989).

[20] D.M. Ceperley and B.J. Alder, Phys. Rev. B **36**, 2092 (1987).

[21] S.M. Younger, Phys. Rev. A **45**, 8657 (1992); in *Radiative Properties of Hot Dense Matter*, edited by W. Goldstein, C. Hooper, J. Gauthier, J. Seely, and R. Lee (World Scientific, Singapore, 1991), p. 137.

[22] J. Theilhaber, Phys. Fluids B **4**, 2044 (1992); Phys. Rev. B **46**, 12 990 (1992).

[23] D. Hohl, V. Natoli, D.M. Ceperley, and R.M. Martin, Phys. Rev. Lett. **71**, 541 (1993); M.P. Grumbach, D. Hohl, R.M. Martin, and R. Car, J. Phys. Condens. Matter **6**, 1999 (1994).

[24] G. Zèrah, J. Clérouin, and E.L. Pollock, Phys. Rev. Lett. **69**, 446 (1992); J. Clérouin, E.L. Pollock, and G. Zèrah, Phys. Rev. A **46**, 5130 (1992); J.I. Penman, J. Clérouin, and G. Zèrah, Phys. Rev. E **51**, R5224 (1995).

[25] I. Kwon, L. Collins, J. Kress, N. Troullier, and D. Lynch, Phys. Rev. E **49**, R4771 (1994).

[26] I. Kwon, J. Kress, and L. Collins, Phys. Rev. B **50**, 9118 (1994); L. Collins, J. Kress, I. Kwon, D. Lynch, and N. Troullier, in *Atomic Processes in Plasmas*, edited by W.L. Rowan, AIP Conf. Proc. No. 322 (AIP, New York, 1995), p. 187.

[27] V.E. Fortov and I.T. Iakubov, *Physics of Nonideal Plasma* (Hemisphere, New York, 1990).

[28] C. Pierleoni, D.M. Ceperley, B. Bernu, and W.R. Magro, Phys. Rev. Lett. **73**, 2145 (1994).

[29] M. Topaler and N. Makri, J. Chem. Phys. **97**, 9001 (1992).

[30] M.P. Allen and D.J. Tildesley, *Computer Simulation of Liquids* (Oxford Science, Oxford, 1987); J.M. Haile, *Molecular Dynamics Simulations* (Wiley, New York, 1992).

[31] J.P. Hansen, and I.R. McDonald, *Theory of Simple Liquids* (Academic, San Diego, 1986).

[32] N.H. March and M.P. Tosi, *Atomic Dynamics in Liquids*, (Macmillan, London, 1976).

[33] M. Schoen and C. Hoheisel, Mol. Phys. **52**, 33 (1984); **52**, 1029 (1984).

[34] G. Jacucci and I.R. McDonald, Physica (Amsterdam) **80A**, 607 (1975).

[35] R.G. Parr and W. Yang, *Density Functional Theory of Atoms and Molecules* (Oxford University, Oxford, 1989).

[36] D.K. Remler and P.A. Madden, Mol. Phys. **70**, 921 (1990); M.C. Payne, M.P Teter, D.C. Allen, T.A, Arias, and J.D. Joannopoulos, Rev. Mod. Phys. **64**, 1045 (1992).

[37] N.D. Mermin, Phys. Rev. **137**, A1441 (1965).

[38] R. Wentzcovitch, J.L. Martins, and P.B. Allen, Phys. Rev. B **45**, 11372 (1992); R.M. Wentzcovitch and J.L. Martins, Solid State Commun. **78**, 831 (1991).

[39] J.P. Perdew and A. Zunger, Phys. Rev. B **23**, 5048(1981).

[40] D.M. Ceperley and B.J. Alder, Phys. Rev. Lett. **45**, 566(1980).

[41] N. Troullier and J.L. Martins, Phys. Rev. B **43**, 1993 (1991).

[42] L. Kleinman and D.M. Bylander, Phys. Rev. Lett. **48**, 1425 (1982).

[43] C.G. Broyden, Math. Comp. **19**, 577 (1965).

[44] E.R. Davidson, Comput. Phys. **7**, 521 (1993), and references therein.

[45] W.A. Harrison, *Solid State Theory* (McGraw-Hill, New York, 1970).

[46] N.W. Ashcroft and N.D. Mermin, *Solid State Physics* (Saunders, Philadelphia, 1976).

[47] I.M. Torres, *Interatomic Potentials* (Academic, New York, 1972).

[48] J. Erpenbeck, Phys. Rev. A **35**, 218 (1987).

[49] R.A. Aziz and M.J. Slaman, J. Chem. Phys. **94**, 8047 (1991).

[50] D.L. Lynch, N. Troullier, J.D. Kress, and L. Collins, J. Chem. Phys. **101**, 7048 (1994).

[51] T.W. Barbee and M.L. Cohen, Phys. Rev. B **44**, 11 563 (1991).

[52] B. Holian (private communication).

[53] R. Friedberg and J.E. Cameron, J. Chem. Phys. **52**, 6049 (1970).

[54] R. Car and M. Parrinello, Phys. Rev. Lett. **55**, 2471 (1985).

[55] Z. Lin and J. Harris, J. Phys. Condens. Matter **4**, 1055 (1992).

[56] J. Kress, I. Kwon, and L. Collins, J. Quantum Spectrosc. Radiat. Transfer **54**, 237 (1995).

[57] H.S.W. Massey, *Electronic and Ionic Impact Phenomena: Slow Collisions of Heavy Particles* (Oxford University, Oxford, 1971), p. 1422.

[58] P. Siegbahn and B. Liu, J. Chem. Phys. **68**, 2457 (1978).

[59] I. Kwon, L. Collins, J. Kress, and N. Troullier, Europhys. Lett. **29**, 537 (1995).